ACS Catalysis

Research Article

pubs.acs.org/acscatalysis

Mo_2C/Graphene Nanocomposite As a Hydrodeoxygenation Catalyst for the Production of Diesel Range Hydrocarbons

Seok Ki Kim,[†,§] Dohyeon Yoon,[‡] Seung-Cheol Lee,[§] and Jaehoon Kim*[,‡,∥]

[†]Clean Energy Research Center, Korea Institute of Science and Technology, Hwarangno 14-gil 5, Seongbuk-gu, Seoul 136-791, Republic of Korea

[‡]School of Mechanical Engineering, Sungkyunkwan University, 2066, Seobu-Ro, Jangan-Gu, Suwon, Gyeonggi-Do 440-746, Republic of Korea

[§]Electronic Materials Research Center, Korea Institute of Science and Technology, Hwarangno 14-gil 5, Seongbuk-gu, Seoul 136-791, Republic of Korea

[∥]Sungkyun Advanced Institute of Nano Technology (SAINT), Sungkyunkwan University, 2066, Seobu-Ro, Jangan-Gu, Suwon, Gyeong Gi-Do 440-746, Republic of Korea

Supporting Information

ABSTRACT: Carbon-supported Mo_2C nanoparticles were synthesized and used as catalysts for the deoxygenation of oleic acid and soybean oil to produce diesel-range hydrocarbons. Various carbon materials, such as reduced graphene oxide (RGO), glassy spherical carbon (SC), activated carbon (AC), and mesoporous carbon (MC), were used as supports to determine the effects of RGO in the deoxygenation reactions. The effects of the flow rate, Mo content of the catalyst, and the structure of the carbon support on the conversion and product selectivity were investigated. The morphology analysis revealed that Mo_2C nanoparticles were well-dispersed onto the RGO (Mo_2C/RGO). Under moderate reaction condition (T = 350 °C, P = 5.0 MPa, H_2/oil ratio = 4.5, LHSV = 2 h^{-1}), oleic acid was efficiently deoxygenated using the Mo_2C/RGO catalyst, which produced hydrocarbons with ≥85% yield and ≥90% hydrocarbon selectivity. This value was much higher than those obtained using the Mo_2C/SC, Mo_2C/AC, and Mo_2C/MC catalysts (yields = 18.5−50.3%) under identical conditions. The higher catalytic activity of the RGO-supported catalyst originated from its large pore size, which facilitated transport of the reactants, and uniform deposition of the Mo_2C nanoparticles on the RGO surface. Even over a short contact time (LHSV = 8 h^{-1}) and using natural triglyceride as a reactant, the Mo_2C/RGO catalyst exhibited ≥40% yield of hydrocarbons, whereas a commercial $CoMoS_x/Al_2O_3$ catalyst produced ≤10% yield under identical conditions. The Mo_2C/RGO catalyst was highly selective toward C−O bond scission in the hydroxyl group, which produced water and hydrocarbons without truncating the carbon skeleton of the starting material. Mo_2C/RGO exhibited a prolonged catalyst lifetime for the deoxygenation of soybean oil (13% decrease in conversion after 6 h), compared with the commercial $CoMoS/Al_2O_3$ catalyst (42% decrease).

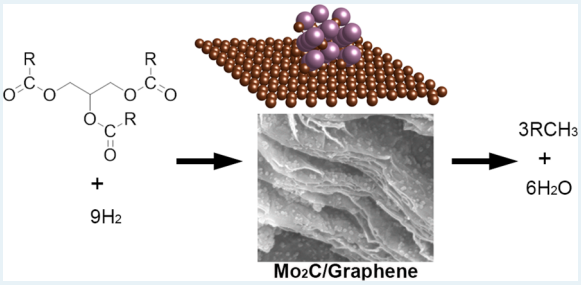

KEYWORDS: *reduced graphene oxide, hydrodeoxygenation, molybdenum carbide, renewable fuel, fatty acid*

INTRODUCTION

The development of an efficient and economically viable process for the conversion of biomass into liquid hydrocarbons has been extensively studied because of the possibility of an eventual exhaustion of petroleum resources, the rapidly increasing demand for transportation, and to mitigate the emission of greenhouse gases. The catalytic deoxygenation of natural triglycerides to produce diesel-like hydrocarbons is the process closest to commercialization because of its potential application in the current petroleum refinery infrastructure.[1−3] Other advantages, such as the absence of metallic or acidic impurities, high energy density, and oxygen stability, have made renewable hydrocarbons, synthesized by deoxygenation of natural triglycerides, more amenable for replacing petroleum diesel, compared with the existing fatty acid esters that are obtained by transesterification.[4] Nevertheless, a number of drawbacks remain unresolved: excessive hydrogen consumption, harsh reaction conditions, rapid catalyst deactivation, and the environmentally hostile byproducts of sulfur-containing catalysts.[5] Therefore, considerable effort is being made to develop a highly active, reliable, and environmentally benign catalytic deoxygenation process that can produce a high yield of diesel-range hydrocarbons.

The most widely used catalysts for the deoxygenation of natural triglycerides are Mo-based sulfide catalysts (e.g., $CoMoS/Al_2O_3$ and $NiMoS/Al_2O_3$).[6−9] Although they exhibit

Received: November 6, 2014
Revised: April 10, 2015
Published: April 17, 2015

DOI: 10.1021/acscatal.5b00335
ACS Catal. 2015, 5, 3292−3303

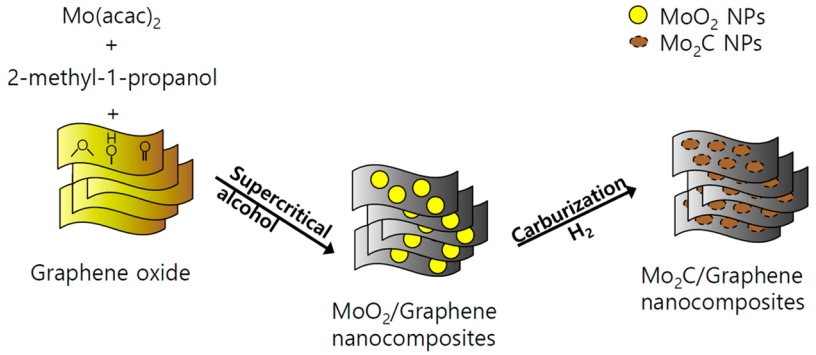

Figure 1. Synthetic procedure for the Mo_2C/RGO catalyst.

a high deoxygenation activity, the use of a toxic sulfur source, such as H_2S, is required to maintain their catalytic activity.[10] This eventually leads to the release of poisonous sulfur compounds into the environment. In this regard, various types of precious-metal catalysts, such as Ir, Ni, Pd, Pt, Rh, and Ru, which are supported on large-surface-area Al_2O_3, SiO_2, or zeolites, have been extensively tested. These catalysts exhibited good deoxygenation activity without requiring the use of sulfides.[11−15] The advantage of using a precious-metal catalyst is the minimization of hydrogen consumption due to their predominant decarboxylation or decarbonylation activity, in which oxygen atoms are removed through the formation of CO_2 or CO, respectively.[16] However, the major drawbacks of the supported metal catalysts are numerous side-reactions, such as double-bond saturation, methanation, hydrocracking, and reverse water−gas shift reaction if the reaction conditions are not carefully optimized, and this often results in a decrease in the selectivity for the targeted hydrocarbons accompanied by unexpected hydrogen consumption.[14,17] In addition, the high cost and scarcity of precious metals have prompted the development of new catalysts that consist of earth-abundant materials.

Among the catalysts recently developed for deoxygenation, Mo_2C catalysts have shown potential usefulness because of their high activity of C−O bond scission and isomerization without causing an extensive saturation of the double bonds present in fatty acids. For example, Ren et al. found that porous Mo_2C selectively converted C_3 oxygenates into an unsaturated hydrocarbon, that is, propylene, even in a hydrogen-rich atmosphere (H_2/reactant = 10 mole fraction).[18] Han et al. synthesized Mo_2C nanoparticles (NPs) supported by various carbon substrates, that is, activated carbon, carbon nanotubes, and ordered mesoporous carbon, for the hydrodeoxygenation of various natural triglycerides with a high selectivity for branched hydrocarbons (85−95% of the total hydrocarbon yield) in a hydrogen-rich atmosphere (H_2/oil = 120−720 mole fraction).[19−21] Although these and other developments in Mo_2C catalysts[18−24] are invaluable, the roles of the Mo_2C nanostructure, the supporting material, and their synergetic effect on the hydrodeoxygenation of natural triglycerides are still unclear, particularly with respect to the relative rates of individual reactions, including saturation, hydrodeoxygenation, and hydrocracking, etc.

Herein, Mo_2C NPs supported on reduced graphene oxide (Mo_2C/RGO) were synthesized via a supercritical alcohol route, and the synergetic effect of the Mo_2C-graphene nanocomposite on the deoxygenation of triglycerides was systemically investigated using a continuous-flow fixed-bed reactor. Graphene has distinguished electrical, optical, and chemical properties[25,26] and thus has been widely studied as a potential material for a broad range of applications, which include electronic devices,[27] optical devices,[28] hydrogen storage,[29−31] and Li^+ ion storage.[32] In addition, the high theoretical specific surface area (~2600 m^2/g) and the locally conjugated structure, which promotes surface adsorption, have made graphene a highly desirable material for catalytic applications.[33] However, graphene has not been explored as a support for hydrogenation or deoxygenation catalysts, with the exception of electro- or photocatalyst applications. To elucidate the beneficial effects of graphene as a support, the catalytic performance of Mo_2C/RGO for the deoxygenation of oleic acid (OA, a probe molecule of triglycerides) was compared with Mo_2C NPs supported by other carbon substrates, that is, activated carbon, AC; mesoporous carbon, MC; and glassy spherical carbon, SC. The effect of the space velocity of the reactants on the reaction intermediates was investigated to elucidate the reaction pathway of the deoxygenation of OA over the Mo_2C/carbon catalysts. In addition, catalyst deactivation during the deoxygenation of a natural triglyceride, that is, soybean oil, using either Mo_2C/RGO or a conventional $CoMoS/Al_2O_3$ catalyst, was examined in a continuous flow reactor to assess the practical applicability of the Mo_2C/RGO nanocomposite.

METHOD

Catalyst Preparation. The synthesis of the Mo_2C/carbon catalysts was developed and optimized in the present study. The preparation method involved the following three sequential steps: (1) the oxidative treatment of the carbon surface, (2) the deposition of MoO_2 NPs onto the carbon surface via the supercritical alcohol route, and (3) a carbothermal hydrogen reduction (CHR) to transform the MoO_2 NPs into Mo_2C NPs. This procedure is illustrated in Figure 1.

To prepare graphene oxide (GO), graphite powder (325 mesh, Sigma-Aldrich) was chemically exfoliated using a modified Hummer's method.[34,35] Three other conventional carbon substrates (AC, particle size = 150 μm, Sigma-Aldrich; SC, particle size = 2−12 μm, Sigma-Aldrich; and MC, particle size < 500 nm, Sigma-Aldrich) were oxidized in boiling concentrated nitric acid for 1 h. All the oxidized carbon supports were washed with distilled water until the filtrate was clear and had a neutral pH.

To simultaneously deposit MoO_2 NPs and remove the oxygen functionalities on the carbon support surface, a calculated amount (0.025−0.50 g) of molybdenyl acetylaceto-

DOI: 10.1021/acscatal.5b00335
ACS Catal. 2015, 5, 3292−3303

nate ($MoO_2(acac)_2$, Sigma-Aldrich) was dissolved in 6 mL of 2-methyl-1-propanol (HPLC grade, Sigma-Aldrich). Subsequently, the oxidized carbon support (0.30 g) was dispersed in the $MoO_2(acac)_2$ solution using ultrasonication for 1 h to produce a suspension. The suspension was then introduced into an 11 mL Hastelloy C-276 reactor. After the reactor was sealed, it was immersed in a molten salt bath ($KNO_3/NaNO_3/Ca(NO_3)_2$, 46:24:30, w/w/w) that was held at a constant temperature of 400 °C for 30 min and subjected to horizontal shaking, which reduced the oxidized carbon substrates and transformed the $MoO_2(acac)_2$ into MoO_2. After the supercritical reaction was completed, the reactor was cooled to an ambient temperature by immersing it in a water bath. The MoO_2/C suspension was centrifuged, washed, and filtered through a nylon filter paper (Pall Corp.) with methanol to remove soluble impurities and then vacuum-dried in an oven at 70 °C for 24 h.

The carburization step was conducted using a CHR method. The dried MoO_2/C sample was heated in a tubular furnace, with a H_2 flow rate of 50 mL/min, using a two-step heating ramp procedure. It was heated from ambient temperature to 450 °C at 5 °C/min, and then to 650 °C at 1 °C/min, where it was maintained for 2 h.

The $CoMo/Al_2O_3$ catalyst (2.8 wt % Co and 7.6 wt % Mo; BET surface area = 246.1 m^2/g) that was used for activity comparison was purchased from Strem Chemicals. Before it was used in the deoxygenation reaction, sulfurization was performed under flowing 15% H_2S/H_2 (v/v, flow rate = 50 mL/min) at 400 °C for 2 h.

Deoxygenation. The activity of the catalysts for the deoxygenation of oleic acid (OA, > 99%, Kanto Chemical) was evaluated at 350 °C under 5.0 MPa of H_2 in a fixed-bed reactor (350 mm × 7 mm id, volume = 13.46 mL) containing 0.5 g of catalyst. The reaction condition was set to ensure sufficient hydrocarbon yield to investigate catalytic activity based on previous results.[36] Figure S1 shows the schematic of the reaction system. The catalyst bed was located in the center of the reactor, and its volume was adjusted to 3.95 mL for each catalyst using inert SiC powder (400 mesh, Sigma-Aldrich). The catalyst was activated under flowing H_2 at 400 °C for 1 h before the deoxygenation reaction. The liquid hourly space velocity (LHSV) of OA was varied from 2.0 to 8.0 h^{-1} to control the OA conversion, and the H_2/OA molar ratio was fixed at 4.5. The reaction products were analyzed using an online GC (HP 7890, Agilent) equipped with a flame-ionization detector and a capillary column (DB-5, 30 m × 0.25 mm id, 0.25 μm film thickness, Agilent).

To evaluate the catalyst activity for only the deoxygenation reaction, the hydrogen consumed through the hydrogenation of the hydrocarbon chains was excluded in the calculation of OA conversion (%), obtained by subtracting the sum of the amount of stearic acid (SA) and OA in the product stream from the amount of OA in the reactant stream using the following equation:

$$\text{OA conversion}(\%) = \frac{R_{OA} - (P_{OA} + P_{SA})}{R_{OA}} \times 100$$

where, R_{OA} and P_{OA} are the moles of OA in the reactant and product, respectively, and P_{SA} is the moles of SA in the product. We note that the saturation and hydrocracking reactions producing SA and fatty acids with smaller carbon chains, respectively, were negligible over the series of reactions conducted using the Mo_2C catalysts.

The selectivity of product A, S_A, is given by

$$S_A(\%) = \frac{P_A}{R_{OA} - (P_{OA} + P_{SA})} \times 100$$

where P_A is the moles of A in the product stream.

The hydrocarbon (HC) yield was calculated using

$$\text{HC yield}\ (\%) = \frac{\text{OA conversion} \times S_{HC}}{100}$$

where S_{HC} is the selectivity for hydrocarbons.

The catalytic activity for the deoxygenation of soybean oil (99.9%, MW: 876.38 g/mol, CJ Cheil Jedang Co.) was also tested using the reactor setup described previously. The LHSV for the soybean oil was 2.0 h^{-1} using a fixed H_2/oil molar ratio of 30. The liquid product of this reaction was analyzed using a simulated distillation-GC (Arnel 3023, Clarus 600, Perkin-Elmer) according to ASTM D-7213.[37] From the distillation profiles, the hydrotreating conversion was defined as the percentage of the heavy fraction of the feed that was converted into lighter products during the hydrotreatment:

$$\text{hydrotreating conversion}(\%) = \frac{\text{reactant}^{360+} - \text{product}^{360+}}{\text{reactant}^{360+}} \times 100$$

where reactant^{360+} and product^{360+} are the weight fractions of the components with boiling points greater than 360 °C in the feed and product, respectively.

The gasoline, jet fuel, and diesel selectivities were defined on the basis of their boiling point ranges:

$$\text{gasoline selectivity}(\%) = \frac{\text{product}^{40-200} - \text{reactant}^{40-200}}{\text{reactant}^{360+} - \text{product}^{360+}} \times 100$$

$$\text{jet fuel selectivity}(\%) = \frac{\text{product}^{170-270} - \text{reactant}^{170-270}}{\text{reactant}^{360+} - \text{product}^{360+}} \times 100$$

$$\text{diesel selectivity}(\%) = \frac{\text{product}^{180-360} - \text{reactant}^{180-360}}{\text{reactant}^{360+} - \text{product}^{360+}} \times 100$$

where reactant^{n-m} and product^{n-m} are the weight fractions of the components with boiling points between n and m °C in the feed and product, respectively, that is, gasoline, 40−200 °C; jet fuel, 170−270 °C; and diesel, 180−360 °C.

Characterization. The amount of Mo deposited on the carbon substrates was measured using an inductively coupled plasma-atomic emission spectrometer (ICP-AES, PerkinElmer) after pretreatment with nitric acid at 90 °C for 12 h. X-ray photoelectron spectroscopy (XPS, PHI 5000 Versaprobe, ULVAC-PHI) was performed using monochromated Al Kα X-rays at 1486.6 eV under ultrahigh vacuum conditions. The survey and high-resolution scans were acquired with pass energies of 117.40 and 23.50 eV, respectively.

The structure and crystallite size of the Mo_2C/C catalysts were analyzed using powder X-ray diffraction patterns (XRD,

DOI: 10.1021/acscatal.5b00335
ACS Catal. 2015, 5, 3292−3303

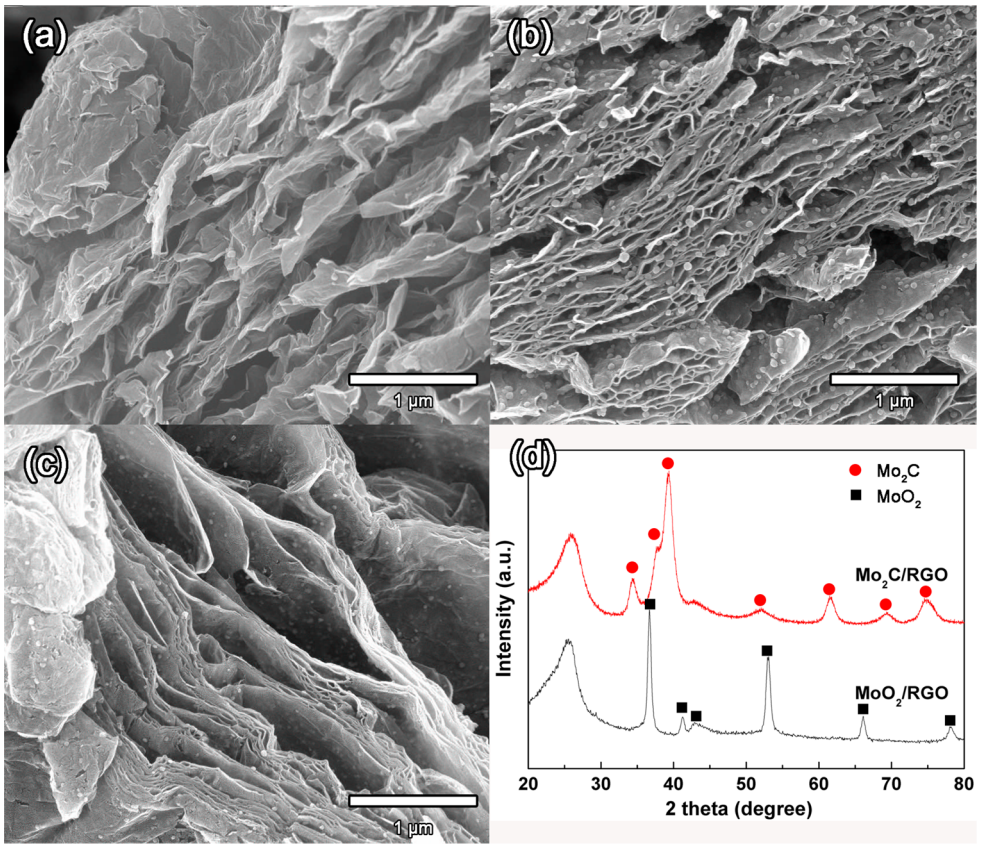

Figure 2. SEM images of (a) RGO, (b) 17 wt % MoO_2/RGO, (c) 17 wt % Mo_2C/RGO, and (d) the XRD patterns of 17 wt % MoO_2/RGO and 17 wt % Mo_2C/RGO.

D/Max-2500 V/PC, Rigaku). The morphology of the catalysts was observed using a field emission scanning electron microscope (S-4100, Hitachi) and a high-resolution transmission electron microscope (HR-TEM, Tecnai-G2, FEI). For the HR-TEM measurements, the samples were dispersed in dimethylformamide using ultrasonication, and then dropped onto a copper grid with a perforated carbon film. The Brunauer–Emmett–Teller (BET) surface area, total pore volume (using N_2 at P/P_0 = 0.99), and the Barrett–Joyner–Halenda (BJH) pore-size distribution were measured using a Belsorp-mini II (BEL) apparatus.

The amount of CO adsorbed onto the catalyst surface was measured using a pulsed titration technique with a BELCAT-B catalyst analyzer (BEL) equipped with a thermal conductivity detector (TCD). A 0.05 g sample of the catalyst was pretreated under flowing H_2 at 400 °C for 1 h and then cooled under flowing He. The flow rates for both the H_2 and He in the pretreatment step were 25 mL/min. Afterward, CO (17 mmol) was injected every 10 min onto the sample catalyst at ambient temperature under a constant He flow rate of 40 mL/min until the saturation of the surface with CO was confirmed using the TCD. The data were processed to calculate the amount of CO adsorbed per gram of catalyst.

Computational Details. The calculation of the free energies for the dissociative adsorption of H_2 onto the carbon and Mo_2C (100) surfaces were performed using density functional theory (DFT) with a plane-wave basis set implemented in the Vienna ab initio simulation package[38,39] with a kinetic cutoff energy of 350.0 eV. The interactions between the ions and electrons were modeled using projector-augmented wave potentials[40] with Perdew–Burke–Ernzerhof exchange-correlation functional[41] parametrization within a generalized gradient approximation. The Kohn–Sham equations were solved self-consistently using an iterative matrix diagonalization scheme.[42] The van der Waals interactions resulting from the dynamic correlations between fluctuating charge distributions were included in these calculations according to the DFT-D2 method,[43] within 35.0 Å of the cutoff radius for pair interactions. The global scaling factor and damping parameter were set to 0.75 and 20.0, respectively. The dispersion coefficient and van der Waals radii of C, H, and Mo were adopted from those used in the empirical force-field.[43] The convergence criterion for the electron density between the electronic steps was 1×10^{-4} eV for all calculations.

The surface structures for graphene and graphite models were generated on the basis of bulk graphite. The lattice parameter of bulk graphite was estimated to be 2.462 Å (C–C bond length = 1.423 Å) with an interlayer distance of 3.160 Å. This value was lower than the real interlayer distance of 3.35 Å. This indicated that the DFT-D2 method has some degree of limitation when describing van der Waals interactions between carbon layers. Other carbon allotropes (sp^2 + sp^3 hybridization), which contrast with graphene (sp^2 hybridization only), were modeled by intercalating carbon atoms with 1/8 or 1/4 monolayer (ML) between the graphite layers. This caused an expansion of the lattice constant from that of pure graphite to 2.523 and 2.563 Å, with reduced interlayer distances of 3.107 and 3.001 Å for 1/8 and 1/4 ML, respectively. A 2 × 2 surface unit cell for graphene was used in the modeling. The graphene was modeled as a fully relaxed, single layer of graphite with a

DOI: 10.1021/acscatal.5b00335
ACS Catal. 2015, 5, 3292–3303

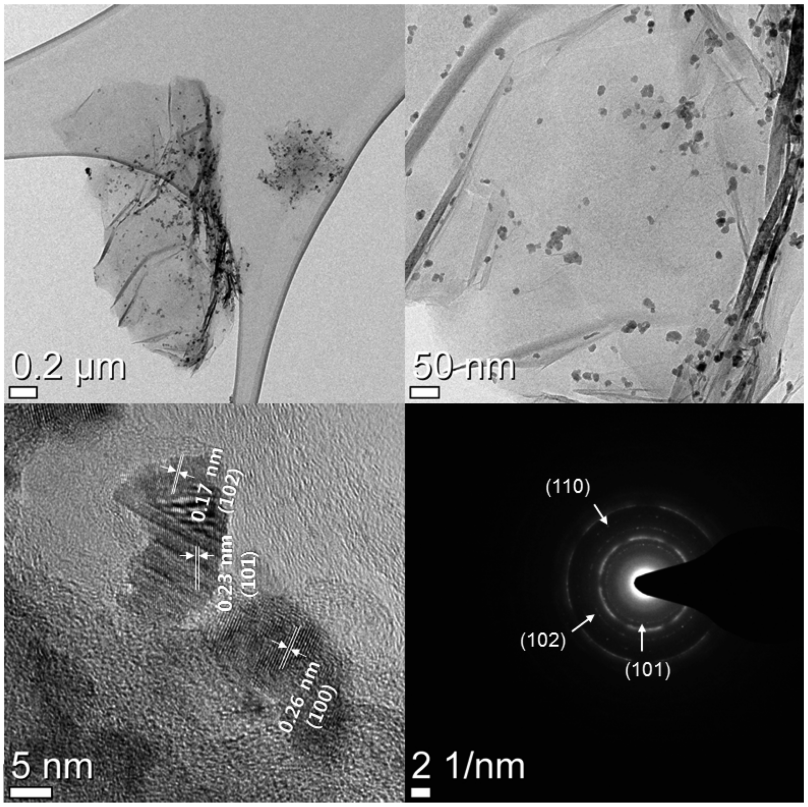

Figure 3. HR-TEM images and the selective area diffraction pattern of 17 wt % Mo_2C/RGO.

12-Å vacuum. The graphite and the 1/8 ML and 1/4 ML-carbon-intercalated graphites were modeled using slabs of four carbon layers separated by 12-Å vacuums. The top two layers were allowed to fully relax during the geometry optimization, whereas the bottom two layers were fixed at the theoretical bulk-terminated geometry. All calculations were performed using the Γ-centered Monkhorst−Pack grids of 8 × 8 × 1 for *k*-point sampling except those for the bulk calculations. The lattice constants obtained from the bulk α-Mo_2C (orthorhombic, *Pbcn*) calculation were a = 4.74, b = 6.05, and c = 5.22 Å, which were very close to the experimentally determined values (a = 4.73, b = 6.02, and c = 5.20).[44] A metal-terminated α-Mo_2C (100) slab (4 × 4 × 3 metal unit cell) with a periodic repetition was employed for the surface. The top two layers of the Mo_2C slab were fully relaxed, whereas the bottom layer was fixed.

RESULTS AND DISCUSSION

Synthesis of Mo_2C/Carbon Nanocomposite. Figure 1 is a schematic diagram for the preparation of the Mo_2C/RGO catalyst using the supercritical alcohol route, followed by CHR. During the supercritical alcohol reaction, the oxygen functionalities of GO were removed, and $MoO_2(acac)_2$ was simultaneously transformed into MoO_2 NPs near the surface of the RGO by a heterogeneous nucleation and growth mechanism. The oxygen functional groups of the chemically exfoliated GO enhanced its interaction with the Mo precursor ($MoO_2(acac)_2$) and resulted in the formation of well-dispersed NPs on the carbon surfaces.[45] The C 1s spectra of GO, MoO_2/RGO, and Mo_2C/RGO that were obtained using X-ray photoelectron spectroscopy (Figure S2) indicated that most of the oxygen functionalities were removed during the supercritical reaction because of the previously reported reducing ability of supercritical alcohols.[46,47] Therefore, the reduction of GO and the deposition of MoO_2 NPs on RGO sheets could be achieved in a single step.

The resultant MoO_2/RGO nanocomposites were subjected to CHR, which converted the MoO_2 NPs into Mo_2C NPs through the migration of carbon atoms from the RGO.[20] The scanning electron microscopy (SEM) images of RGO, MoO_2/RGO, and Mo_2C/RGO and the XRD patterns of MoO_2/RGO and Mo_2C/RGO are shown in Figure 2. The XRD patterns confirmed that phase-pure MoO_2 NPs (2θ = 36.8°, 41.3°, 42.9°, 53.4°, 66.3°, and 78.4°) were formed during the supercritical alcohol reaction and that the MoO_2 NPs were successfully transformed into Mo_2C NPs (2θ = 34.3°, 37.7°, 39.4°, 52.2°, 61.6°, 69.2°, and 74.7°) after the CHR. The crystallite sizes of Mo_2C and MoO_2 NPs were calculated using the XRD patterns and the Scherrer equation. Interestingly, the Mo_2C NPs had a smaller crystallite size (8.7 nm) than the MoO_2 NPs (17.1 nm), which might originate from individual particle reconstruction by replacement of lattice oxygen by carbon during the CHR. A reduction of the particle size during the transformation from MoO_2 to Mo_2C was observed in the SEM images (Figure 2b,c).

To investigate the effect of Mo content on the particle size and its accompanying catalytic activity, Mo_2C/RGO composites with varying Mo contents were prepared. Figure S3 shows the relationship between the measured and intended amount of Mo in the Mo_2C/RGO composites. The actual Mo deposition was up to 14 wt % higher than the intended amount because of weight loss from the substrate, which resulted from the removal of the oxygen functionalities present in GO. However, the actual Mo content was limited to 38 wt % for a 50 wt % $MoO_2(acac)_2$ suspension. In this case, the surface area of RGO might not be large enough to support such a large Mo content,

DOI: 10.1021/acscatal.5b00335
ACS Catal. 2015, 5, 3292−3303

Table 1. BET Surface Areas, Total Pore Volumes, CO Uptakes, and Mo_2C Crystallite Sizes for the Mo_2C/C Catalysts[a]

catalyst[b]	BET surface area (m^2/g_{cat})[c]	BET surface area ($m^2/g_{support}$)[d]	total pore vol (cm^3/g_{cat})[c]	total pore vol ($cm^3/g_{support}$)[d]	av pore size (nm)[e]	CO uptake ($\mu mol/g_{cat}$)[c]	CO uptake ($\mu mol/g_{Mo}$)[f]	crystallite size[g] (nm)
RGO	223.1	223.1	0.81	0.81	7.2			
2 wt % Mo_2C/RGO	205.6	209.8	0.82	0.84	7.9	1.7	85.0	
8 wt % Mo_2C/RGO	171.9	186.8	0.75	0.82	8.7	25.5	318.7	6.7
12 wt % Mo_2C/RGO	148.7	169.0	0.77	0.87	10.3	39.6	330.0	6.7
17 wt % Mo_2C/RGO	133.5	160.8	0.65	0.78	9.7	50.3	295.9	8.7
20 wt % Mo_2C/RGO	126.6	158.3	0.60	0.75	9.4	56.9	284.5	10.4
38 wt % Mo_2C/RGO	103.3	166.6	0.62	1.00	12.0	79.8	210.0	10.9
SC	1.03	1.03						
17 wt % Mo_2C/SC	1.00	1.24				13.3	78.2	25.0
AC	748.9	748.9	0.53	0.53	1.4			
17 wt % Mo_2C/AC	604.9	728.8	0.44	0.53	1.4	52.5	308.8	11.1
MC	204.8	204.8	0.34	0.34	3.3			
17 wt % Mo_2C/MC	140.9	169.8	0.19	0.41	2.7	46.9	275.8	4.7

[a]Below the detection limit if no value reported. [b]x wt % refers to the Mo content. [c]Calculated on the basis of weight (g) of the catalyst. [d]Calculated on the basis of weight (g) of the support. [e]Using a slit-like pore model. [f]Calculated on the basis of weight (g) of Mo. [g]Calculated using the Scherrer equation and the XRD patterns.

which canceled out the effect of the oxygen removal. As shown in Figure 3 and Figure S4, well-dispersed Mo_2C NPs were deposited onto the surface of RGO.

Mo_2C NPs were also deposited onto other carbon substrates, that is, SC, AC, and MC, using a similar procedure. Their actual Mo contents were adjusted to 17 wt % to compare to the optimum hydrocarbon yield obtained using Mo_2C/RGO (vide infra). The SEM images for the Mo_2C/SC, Mo_2C/AC, and Mo_2C/MC composite catalysts are shown in Figure S5. In addition to their deposition on the carbon substrates, some degree of particle agglomeration was observed for the Mo_2C NPs, which is indicated by arrows in the figures.

The BET surface area, CO chemisorption, and Mo_2C crystallite size (that were calculated using the XRD patterns of the samples; Figure S6) are summarized in Table 1. On the basis of a unit weight of the catalyst, the BET surface areas of Mo_2C/RGO (m^2/g_{cat}) and the pore volume (cm^3/g_{cat}) decreased from 223.1 to 103.3 m^2/g, and 0.81 to ~0.60 cm^3/g, respectively, upon increasing the Mo content from 0 to 38 wt %. Because Mo_2C is much denser than the carbon support, increasing the Mo content resulted in a lower surface area and pore volume. Thus, based on a unit weight of the support, the BET surface area ($m^2/g_{support}$), and the pore volume ($cm^3/g_{support}$) were re-estimated, and the results are listed in Table 1. This BET surface area decreased from 223.1 $m^2/g_{support}$ to 160 $m^2/g_{support}$ upon increasing the Mo content from 0 to 17 wt %. A further increase in the Mo content beyond 17 wt % did not result in an additional decrease in the BET surface area of the support. The total pore volume based on a unit weight of the support ($cm^3/g_{support}$) did not show a trend upon increasing the Mo content up to 20 wt %. However, when the Mo content further increased to 38 wt %, a large increase in the total pore volume (1.00 $cm^3/g_{support}$) was observed, which suggested an enlargement of the interlayer space wherein many Mo_2C particles were inserted.

Although the active site of Mo_2C for deoxygenation is not fully understood, previous studies using Mo_2C NPs catalysts for hydrodesulfurization or hydrodenitrogenation showed that CO titration could be used to evaluate the surface exposure of Mo_2C NPs.[48−50] The CO uptake for the Mo_2C/RGO catalysts ($\mu mol/g_{cat}$) increased from 1.7 to 79.8 $\mu mol/g_{cat}$ upon increasing the Mo content from 2 to 38 wt %. When the CO uptakes were re-estimated on the basis of the actual Mo content ($\mu mol/g_{Mo}$), the value increased from 85.0 to 330.0 $\mu mol/g$ upon increasing the Mo content from 2 to 12 wt %, but it then decreased to 210 $\mu mol/g_{Mo}$ upon further increasing the Mo content to 38 wt %. The crystallite size that was calculated from XRD pattern of the Mo_2C increased from 6.7 to 10.9 nm upon increasing the Mo content from 8 to 38 wt %. The relationship between the particle size, CO uptake, and catalytic activity will be discussed in next section.

When other carbon supports were used to prepare the Mo_2C/carbon catalysts, the crystallite size decreased in the following order: Mo_2C/SC (25.0 nm) > Mo_2C/AC (11.1 nm) > Mo_2C/RGO (8.7 nm) > Mo_2C/MC (4.7 nm) at identical Mo contents (17 wt %). The largest crystallite size, which was observed for Mo_2C/SC, was due to the small surface area of the SC (1.03 $m^2\ g^{-1}$) because heterogeneous nucleation of MoO_2 on the surface of the substrate during the supercritical alcohol reaction was limited. This caused extensive homogeneous nucleation of MoO_2 particles in the fluid phase and severe agglomeration, as shown in Figure S5a. A decrease in the BET surface area was observed after Mo_2C content on the AC and MC supporting materials. The CO uptake on Mo_2C/AC and Mo_2C/MC was similar to that of the 17 wt % Mo_2C/RGO, which implied that each catalyst might have similar active sites on the Mo_2C NPs for the hydrodeoxygenation reaction. Thus, the differences in the catalytic activity of these three catalysts resulted from other factors, such as the physicochemical properties of the substrates.

DOI: 10.1021/acscatal.5b00335
ACS Catal. 2015, 5, 3292−3303

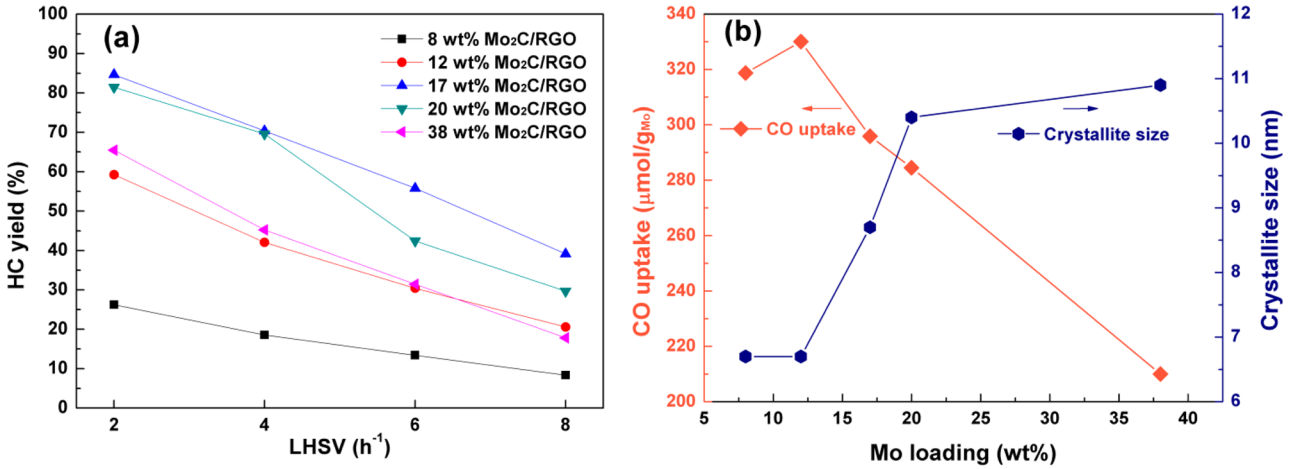

Figure 4. Effect of Mo loading on (a) hydrocarbon (HC) yield at various space velocities (LHSV = 2−8 h^{-1}) and (b) CO uptake (μmol/g_{Mo}) and crystallite size of Mo_2C (nm) calculated using XRD. Reaction conditions: T = 350 °C, P = 5.0 MPa, and H_2/OA molar ratio = 4.5. RGO, reduced graphene oxide.

Deoxygenation. Figure 4a shows the effect of the Mo content on the hydrocarbon (HC) yields at varying LHSVs when using the Mo_2C/RGO catalysts. In each reaction, an identical amount of the Mo_2C/RGO catalysts (0.5 g) was used in the continuous flow fixed bed reactor. The HC yields of the Mo_2C/RGO catalysts showed similar behavior when varying the LHSV from 2−8 h^{-1}. When the Mo content increased from 8 to 17 wt %, the HC yield increased, whereas a further increase in the Mo content to 38 wt % resulted in a decrease in yield. The 17 wt % Mo catalyst showed the best performance and produced hydrocarbon yields between 84.6% and 39.1% at LHSVs from 2 h^{-1} to 8 h^{-1}, respectively.

Figure 4b shows the changes in CO uptake (based on a unit weight of Mo) and the crystallite size of Mo_2C in the Mo_2C/RGO catalysts as a function of the Mo content. The CO uptake on the catalyst (μmol/g_{cat}, Table 1) gradually increased with increasing Mo content, and higher OA conversion and HC yield were expected with a higher Mo content. However, the CO uptake based on unit weight of Mo (μmol/g_{Mo}) decreased with increasing Mo content, which suggested an increase in the Mo_2C particle size. This corresponded to the increase in the measured crystallite sizes shown in Figure 4b. Because the BET surface areas that were based on a unit weight of the support of the 17−38 wt % Mo_2C/RGO catalysts were very similar, the decrease in HC yield for the 20 and 38 wt % Mo_2C/RGO catalysts could be considered a result of the enlargement of the Mo_2C particle size rather than a mass transfer limitation. If the extent of the internal mass transfer among RGO-supported catalysts is assumed to be similar, the intrinsic activity of the different-sized Mo_2C nanoparticles could be compared. The turnover frequencies of the OA deoxygenation over a series of Mo_2C/RGO catalysts (Table 2) indicated that the catalytic activity of Mo_2C decreased with increasing particle size. Therefore, the highest hydrocarbon yield, which was observed for the 17 wt % Mo_2C/RGO, might be due to a sufficient amount of exposed active sites combined with a relatively small Mo_2C particle size to catalyze the OA hydrodeoxygenation reaction.

Figure 5a shows the effect of the carbon substrate on hydrocarbon yields for a fixed Mo content of 17 wt %. The properties of each catalyst, such as specific surface area, CO uptake, pore analyses, and crystallite size, are summarized in Table 1. The hydrocarbon yield increased in the order of Mo_2C/RGO > Mo_2C/AC > Mo_2C/MC > Mo_2C/SC under all LHSV conditions. The low BET surface area, low CO uptake, and large crystallite size of 17 wt % Mo_2C/SC were responsible for its low HC yield. We note that using 17 wt % Mo content was not necessarily optimal for the other carbon substrates. Nevertheless, the Mo_2C/AC and Mo_2C/MC exhibited similar CO uptake values (52.5 μmol/g_{cat}, 308.8 μmol/g_{Mo} and 46.9 μmol/g_{cat}, 275.8 μmol/g_{Mo}, respectively) when compared with Mo_2C/RGO (50.3 μmol/g_{cat}, 295.9 μmol/g_{Mo}). This suggested that the number of exposed active sites was comparable among those three catalysts.

Table 2. Turnover Frequencies (TOFs) for the Deoxygenation of Oleic Acid (OA) over Mo_2C/RGO Catalysts[a,b]

Mo content (wt %)	TOF (s^{-1})
8	0.16
12	0.12
17	0.13
20	0.11
38	0.07

[a]The number of active sites was measured by CO uptake. [b]Reaction condition: T = 350 °C, P = 5.0 MPa, H_2/OA molar ratio = 4.5, and LHSV = 2^{-1}.

The N_2 adsorption−desorption isotherms were examined to elucidate the superior HC yield of the Mo_2C/RGO catalyst (Figure 5b). The shapes of the hysteresis loops indicated that Mo_2C/RGO has a typical slit-like structure without rigid aggregates, whereas the AC- and MC-supported catalysts were composed of narrow slit pores that included micropores.[51] The pore size distributions (Figure 5c) also indicated the presence of a relatively larger portion of meso-to-macro pores with sizes in the range of 10−100 nm and a larger average pore size of 9.7 nm in the Mo_2C/RGO catalyst when compared with Mo_2C/AC and Mo_2C/MC, which had average pore sizes of 1.4−2.7 nm). The other RGO-supported catalysts with various Mo loading (0−38 wt %) showed similar N_2 adsorption−desorption isotherms and pore size distributions, as shown in Figure S7. The presence of larger pores might be responsible for the enhanced OA deoxygenation performance. The limit of the reaction rate within a porous catalyst is closely related to

DOI: 10.1021/acscatal.5b00335
ACS Catal. 2015, 5, 3292−3303

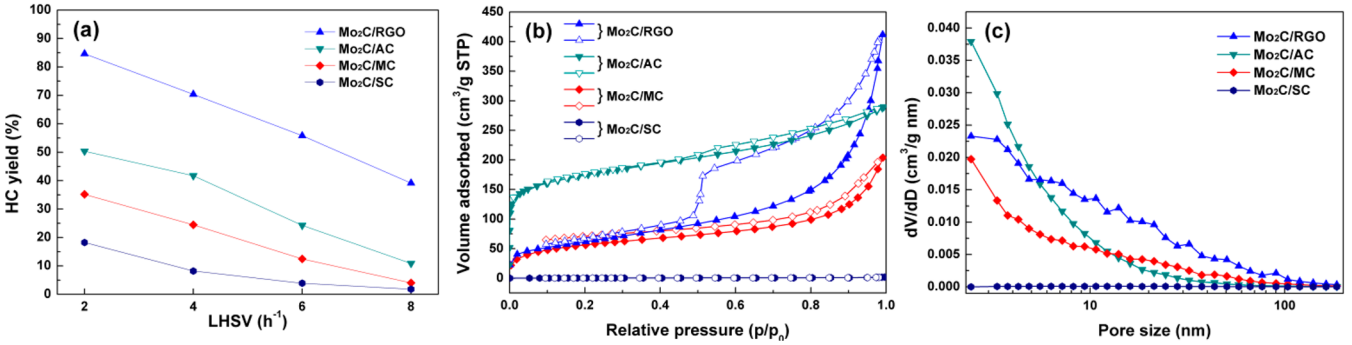

Figure 5. Effect of the carbon support on (a) hydrocarbon (HC) yield at various space velocities (LHSV = 2−8 h^{-1}), (b) N_2 adsorption−desorption isotherm, and (c) BJH pore size distribution. Reaction conditions: T = 350 °C, P = 5.0 MPa, and H_2/OA molar ratio = 4.5. RGO, reduced graphene oxide; AC, activated carbon; MC, mesoporous carbon; and SC, spherical glassy carbon.

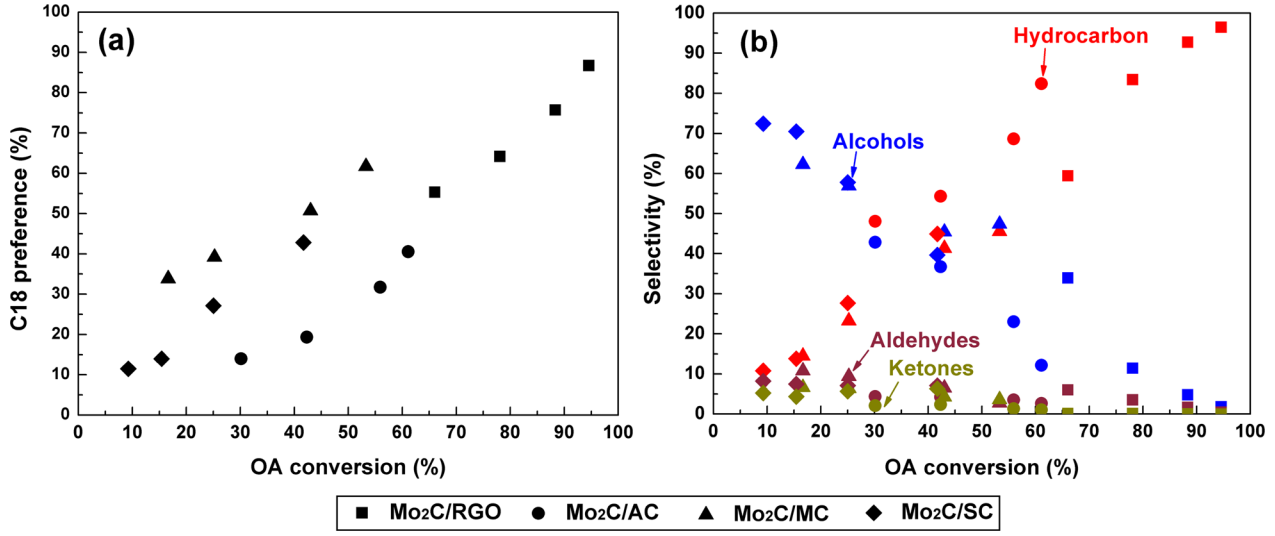

Figure 6. (a) C18 preference (C18/(C17 + C18)) vs oleic acid (OA) conversion. (b) Product selectivities versus OA conversion. RGO, reduced graphene oxide; AC, activated carbon; MC, mesoporous carbon; and SC, spherical glassy carbon.

the size exclusion effect of the pore diameters. The large pore sizes of the Mo_2C/RGO catalyst relative to OA molecules (with a molecular diameter of 0.8 nm) were expected to facilitate internal transport of the OA molecules. In contrast, the pore sizes of Mo_2C/AC and Mo_2C/MC are only 2−3 times larger than the size of OA, which might result in the reaction being limited by the diffusion of the reactants into the pores of the catalysts. Mass transfer limitation issues in the reactions of large molecules, such as triglycerides or fatty acids in which the activities and selectivities were significantly improved by using catalysts with larger pore diameters[52] or by employing supercritical fluid media to enhance the effective diffusivity of the reactant[5] have been previously reported.

Another plausible reason for the improved deoxygenation of OA when using the Mo_2C/RGO catalyst might be the uniform distribution of the nanosized Mo_2C particles onto the surface of the RGO. The GO, which was rich in oxygen functionalities, led to the uniform decoration of Mo_2C nanoparticles onto the RGO surface by enhancing heterogeneous nucleation and growth (Figure 3), and therefore each Mo_2C nanoparticle was readily accessible to perform the deoxygenation reaction. In contrast, the active sites of the micrometer-sized porous Mo_2C aggregates on the AC and MC surfaces (Figure S5), which were formed in the fluid phase by a homogeneous nucleation and growth mechanism, might not be as widely accessible.

Reaction Mechanism. To understand the effect of the carbon substrates on the electronic structures of MoO_2 and Mo_2C, which were supported by RGO, SC, AC, and MC, they were analyzed by XPS (see Figure S8). After the CHR, all of the catalysts showed an increased intensity of the Mo^{2+} peaks because of the formation of Mo_2C from MoO_2. The peak deconvolution results that are listed in Table S1 indicated that the oxidation state of Mo_2C on RGO was similar to that on the other carbon supports. This result suggested that the electronic structure of the Mo_2C/C catalysts was not affected by its carbon support structure.

The oxygen molecules present in OA could be removed by forming either carbon oxides (CO_2 and CO) or H_2O as reaction byproducts. The former two pathways are known as decarboxylation and decarbonylation, respectively, and are the result of C−C bond scission. The latter pathway is known as hydrodeoxygenation and is the result of C−O bond cleavage.[17] The hydrocarbons produced through the decarboxylation or decarbonylation of OA have a carbon chain length of 17 (C17), whereas those produced through hydrodeoxygenation have a carbon chain length of 18 (C18). Here, the ratio of C18/(C17+C18) of the hydrocarbons in the liquid product was designated as the "C18-preference" and was plotted versus the OA conversion when using the Mo_2C/C catalysts, as shown in Figure 6a. All of the catalysts showed a similar trend in that the

DOI: 10.1021/acscatal.5b00335
ACS Catal. 2015, 5, 3292−3303

Scheme 1. Proposed Hydrodeoxygenation Mechanism Using Carbon-Supported Mo_2C Catalysts[a]

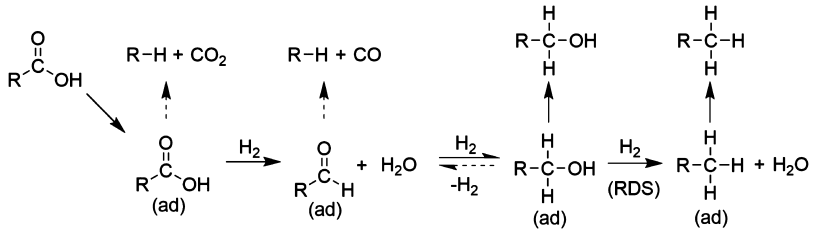

[a]Adsorbed species are denoted as (ad). Unfavorable reactions are shown as dashed arrows.

C18-preference increased with OA conversion. These results suggested that decarboxylation or decarbonylation occurs to some extent under the condition that the OA conversion is low, but hydrodeoxygenation was preferred as the reaction proceeded to high OA conversion under the reaction conditions used herein, that is, 350 °C, H_2 pressure = 5.0 MPa, and H_2/OA = 4.5. Figure 6b shows the changes in product selectivity versus the OA conversion for the Mo_2C/C catalysts. The alcohol species were determined to be the primary reaction intermediate, and the formation of alcohol showed a negative correlation with hydrocarbon production. A similar relationship between hydrocarbon and alcohol selectivity was observed for the other Mo_2C catalysts.

Previous mechanistic studies on the metal-catalyzed deoxygenation of fatty acids in hydrogen-rich atmospheres revealed that the rapid hydrodeoxygenation of carboxylic acids (R−COOH) into their corresponding aldehydes (R−CHO) occurred in the initial stage of the reaction, which was followed by either decarbonylation induced by C−C bond scission (R−CHO → RH + CO), or further hydrogenation to the alcohol ($R-CH_2OH$).[53,54] For the Mo_2C/C catalyst used herein, the initial hydrodeoxygenation to the aldehyde and its subsequent hydrogenation to the alcohol were rapid, as in the case of supported metal catalysts. However, the C−O bond of the alcohol then underwent another hydrodeoxygenation ($R-CH_3 + H_2O$) rather than dehydrogenation to aldehyde followed by decarbonylation. The latter hydrodeoxygenation rate appeared to be slower than the former, which resulted in the accumulation of the intermediate alcohol (see Scheme 1). The observation of a faster C−O bond scission than C−C bond scission when using Mo_2C catalysts was consistent with previous studies.[18,55,56]

As shown in Figure 6, both the C18 preference and the product selectivity changed with the OA conversion, but their differences among the different catalysts were insignificant. This indicated that the deoxygenation mechanism of OA was not strongly affected by the structure of the carbon support, and the deoxygenation reaction occurred mainly on the surface of the Mo_2C nanoparticles, which exhibited similar electronic properties among the different carbon structures, as shown by XPS (see Figure S8 and Table S1).

To elucidate the effect of the carbon supports on the deoxygenation reaction, a series of DFT calculations were performed. Because hydrogen participates in the deoxygenation of OA, the free energies of the dissociative adsorption of hydrogen onto the surface of the catalysts were calculated using the assumption that the hydrogen absorption occurs within the reaction conditions used herein, that is, temperature = 350 °C and pressure = 5.0 MPa. We also assumed that the RGO was composed of only sp^2-hybridized carbon atoms, whereas the other carbon allotropes also contained some sp^3-hybridized carbon atoms. This assumption was supported by the XPS results of the GO and RGO as discussed in the previous section (see Figure S2).

Figure 7 shows every possible adsorption site for hydrogen atoms on the carbon substrates and the Mo_2C (100) surface,

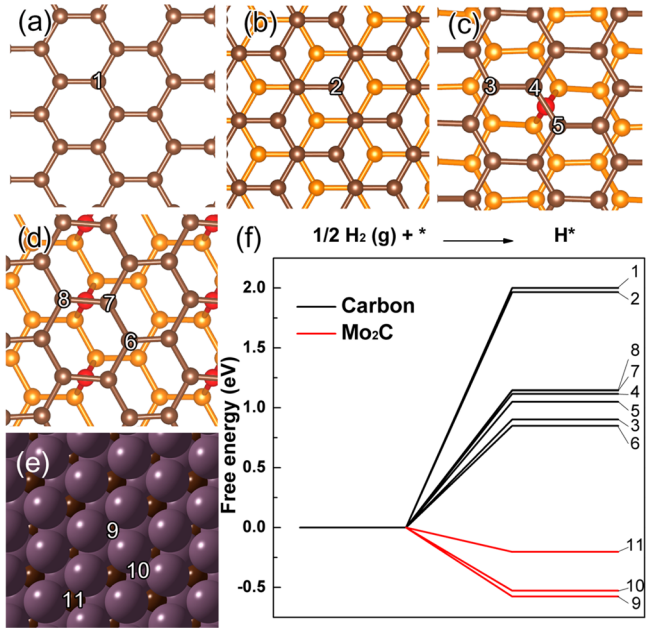

Figure 7. Adsorption sites for atomic hydrogen on (a) graphene, (b) graphite, (c) graphite with 1/8 ML C intercalated, (d) graphite with 1/4 ML C intercalated, and (e) a Mo_2C (100) surface. The first (brown) and second (yellow) layers with intercalated carbon atoms (red) are presented for parts b−d. All structures were taken after relaxation. (f) Free energy of the dissociative adsorption of hydrogen on the corresponding sites at T = 350 °C and P = 5.0 MPa.

which were optimized using DFT calculations, and their corresponding free energies of adsorption. The dissociative adsorption of hydrogen onto graphene and graphite were endergonic processes (+1.9 eV). When carbon atoms were intercalated between graphite sheets with 1/8 and 1/4 ML, the adsorption free energies were lower than those on the graphene and graphite (from +0.84 to +1.1 eV); however, this was still energetically implausible. The adsorption of hydrogen atoms on the three different Mo_2C sites was much more energetically favorable, with free energies of −0.20, −0.52, and −0.57 eV. Therefore, under our reaction conditions, the dissociative adsorption of hydrogen over carbon-supported Mo_2C catalysts should occur only on the Mo_2C surfaces, not onto the carbon substrates, regardless of their structure.

DOI: 10.1021/acscatal.5b00335
ACS Catal. 2015, 5, 3292−3303

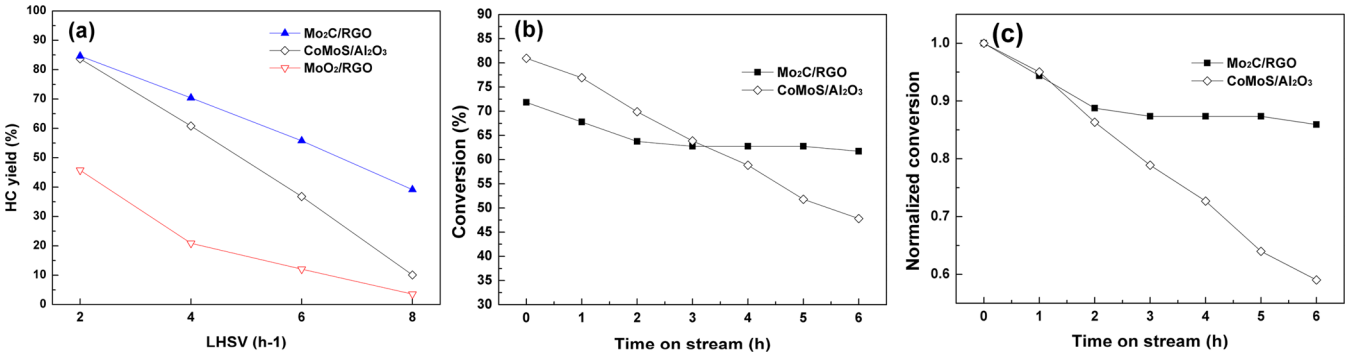

Figure 8. (a) The hydrocarbon (HC) yield obtained using Mo_2C/RGO, $CoMoS/Al_2O_3$, and MoO_2/RGO. Reaction conditions: T = 350 °C, P = 5.0 MPa, and H_2/OA molar ratio = 4.5. (b) Hydrotreating conversion of soybean oil as a function of reaction time for Mo_2C/RGO and $CoMoS/Al_2O_3$. Reaction conditions: T = 350 °C, P = 5.0 MPa, LHSV = 2 h^{-1}, and H_2/soybean oil molar ratio = 30.0. (c) Conversions normalized with initial value.

Table 3. Hydrodeoxygenation Results for the Production of Hydrocarbons Using Various Mo_2C Catalysts

catalyst[a]	feed	reactor type	reaction temp (°C)	H_2/reactant molar ratio[b]	hydrocarbon yield (%)	ref
porous Mo_2C	propanal	fixed-bed	300	10	40−70	18
Mo_2C/CNF	oleic acid + solvent	batch	350	∼30	∼90	22
Mo_2C/RGO	oleic acid	fixed-bed	350	4.5	84.5	this work
Mo_2C/AC	vegetable oil + solvent	batch	280	∼120	76−88	19
Mo_2C/CNT	vegetable oil + solvent	batch	260	∼240	80−87	20
Mo_2C/OMC	vegetable oil + solvent	batch	260	∼720	85−95	21
Mo_2C/Al_2O_3	aunflower oil	fixed-bed	360	∼76	∼100	23
Mo_2C/CNF	vegetable oil + solvent	batch	260	∼300	50−78	24
Mo_2C/RGO	aoybean oil	Fixed-bed	350	30	62−72	this work

[a]CNF, carbon nanofiber; AC, activated carbon; CNT, carbon nanotube; OMC, ordered mesoporous carbon; RGO, reduced graphene oxide. [b]The molar amount of hydrogen was calculated using the ideal gas law based on the corresponding references.

Thus far, no prominent chemical properties of either the Mo_2C or the carbon-support structure have been found that explain the superior performance of the Mo_2C/RGO in the OA deoxygenation. The only meaningful difference between Mo_2C/RGO and the other carbon-supported Mo_2C catalysts was its larger pore size and unique slit-like structure, which allowed the effective transport of the large OA molecules, and its uniform distribution of nanoparticulate Mo_2C. However, more structural characterizations, such as porosity and tortuosity, are required for quantitative investigation on the internal mass transfer limitation of Mo_2C catalysts prepared in the present study.

Deoxygenation of Natural Triglycerides. The catalytic deoxygenation of a natural triglyceride, that is, soybean oil, over the MoO_2/RGO and a commercial $CoMo/Al_2O_3$ catalyst was tested, and the results are shown in Figure 8a. The MoO_2/RGO catalyst was prepared using the same method as the Mo_2C/RGO catalyst but without the CHR step. The $CoMo/Al_2O_3$ catalyst was sulfurized to form $CoMoS_x/Al_2O_3$ using H_2S before the reaction. The MoO_2/RGO catalyst had some deoxygenation activity, but it only resulted in low hydrocarbon yields of 45.7% and 20.8% at LHSVs of 2 and 4 h^{-1}, respectively. The hydrocarbon yield of the $CoMoS_x/Al_2O_3$ catalyst was similar to the Mo_2C/RGO catalyst when the LSHV was 2 h^{-1}; however, at higher LHSVs from 4 to 8 h^{-1}, the HC yields from Mo_2C/RGO were 9.5−29.0% greater than those of the $CoMoS_x/Al_2O_3$ catalyst, which indicated that the Mo_2C/RGO catalyst exhibited higher activities at higher space velocities.

Figure 8b,c shows the deactivation behavior for the Mo_2C/RGO and $CoMoS_x/Al_2O_3$ catalysts during the deoxygenation of soybean oil. The initial hydrotreating conversion obtained using the $CoMoS_x/Al_2O_3$ (80.9%) was higher than that using the Mo_2C/RGO (71.8%). The cracking activity of the Al_2O_3 support might be advantageous during the deoxygenation of large triglyceride molecules. This hypothesis was supported by larger fractions of light hydrocarbons (see Figure S9 for the gasoline and jet yields) in the liquid product of the $CoMoS_x/Al_2O_3$-catalyzed reactions. However, the $CoMoS_x/Al_2O_3$ catalyst was rapidly deactivated and had a hydrotreating conversion of only 47.7% after 6 h, whereas the activity of Mo_2C/RGO catalyst decreased somewhat, with a hydrotreating conversion of 61.7%, although not as much as the CoMoS catalyst, during the same reaction period. The rapid deactivation of the $CoMoS_x/Al_2O_3$ catalyst was attributed to the absence of a source of sulfur in the reactant stream, which was required to maintain the sulfurized phase of the $CoMoS_x$ catalyst,[10] and coke deposition on the active sites.[5] Coke deposition was also considered as a mechanism for the deactivation of the Mo_2C/RGO catalyst.

The usual combustion process used for catalyst regeneration could not be applied to the used Mo_2C/RGO because the carbonaceous RGO would also combust. Because the coke formed during the deoxygenation of the triglyceride is classified as "soft coke", which has a high hydrogen content,[57] alternative methods to the conventional combustion, which include the extraction of the coke species using supercritical fluids[58] or simple oxidation using strong $^{\bullet}OH$ radicals, such as hydrogen peroxide,[59] could be used to recycle the Mo_2C/RGO catalysts. Supercritical fluids, with or without an entrainer to enhance solubility, might be promising media for the removal of coke or coke precursors (or both) deposited onto the surface of used catalysts because of their low viscosity, zero surface tension, high diffusivity, and high solubility of organic species.

DOI: 10.1021/acscatal.5b00335
ACS Catal. 2015, 5, 3292−3303

Finally, previous reports of the production of hydrocarbons via the hydrodeoxygenation of natural triglycerides or their probe molecules using various Mo_2C catalysts are summarized in Table 3. The RGO-supported Mo_2C catalysts prepared herein exhibited hydrocarbon yields comparable to those of the other Mo_2C catalysts, even though a significantly lower hydrogen/reactant molar ratio was used and solvents were not required. This might be because of the efficient transport of hydrogen and reactants from the fluid phase to the active sites of Mo_2C within the RGO support.

CONCLUSION

Herein, Mo_2C/RGO was synthesized using a supercritical alcohol route, which was followed by carbothermal hydrogen reduction. For the hydrodeoxygenation of oleic acid, the use of RGO as the catalyst support resulted in approximately 30−60% higher hydrocarbon yields when compared with other carbon materials under the identical reaction conditions (T = 350 °C, P = 5.0 MPa, H_2/OA molar ratio = 4.5, LSHV = 2 h^{-1}). For the hydrodeoxygenation of soybean oil, the Mo_2C/RGO catalyst also exhibited an ∼19.2% higher yield of hydrocarbons when compared with a commercial sulfurized $CoMoS_x/Al_2O_3$ catalyst (under the same conditions as above except H_2/oil molar ratio = 30.0). The dominant mechanism for the deoxygenation of oleic acid over Mo_2C/RGO was the selective C−O bond scission in the hydroxyl group, producing H_2O as a byproduct, without a reduction of the carbon chain length by C−C bond cleavage. During the deoxygenation of soybean oil for 6 h, the Mo_2C/RGO catalyst exhibited only a 13% decrease in conversion, whereas the commercial sulfurized $CoMoS/Al_2O_3$ catalyst exhibited a 42% decrease in conversion. Physicochemical, morphological, and DFT analyses suggested that the higher hydrocarbon yields for the Mo_2C/RGO catalyst originated from the uniform distribution of active Mo_2C nanoparticles on the support, and the efficient transport of reactants because of its large pore size with a unique slit-like structure, rather than the chemical (or electronic) properties of Mo_2C or the hydrogen absorption on the carbon support.

ASSOCIATED CONTENT

Supporting Information

The following file is available on the ACS Publications Web site at DOI:The following file is available free of charge on the ACS Publications website at DOI: 10.1021/acscatal.5b00335.

Statistical thermodynamics of H adsorption; schematic diagram of reaction system; XPS, ICP-AES, SEM images, XRD patterns; N_2 adsorption−desorption isotherms; pore size distributions of Mo_2C catalysts; and in-depth deactivation data of Mo_2C/RGO and $CoMoS/Al_2O_3$ (PDF)

AUTHOR INFORMATION

Corresponding Author

*E-mail: jaehoonkim@skku.edu.

Notes

The authors declare no competing financial interest.

ACKNOWLEDGMENTS

This work was supported by the New & Renewable Energy Core Technology Program (No. 20143030090940) and the Human Resources Development Program (No. 20124010203270) of the Korea Institute of Energy Technology Evaluation and Planning (KETEP) financed by the Ministry of Trade, Industry, and Energy, Republic of Korea. Additional support from the Supercomputing Center at the Korea Institute of Science and Technology Information, with supercomputing resources and technical support (KSC-2012-C2-08) was also appreciated.

REFERENCES

(1) Corma, A.; Huber, G. W.; Sauvanaud, L.; O'Connor, P. *J. Catal.* **2007**, *247*, 307−327.
(2) Huber, G. W.; Corma, A. *Angew. Chem., Int. Ed.* **2007**, *46*, 7184−7201.
(3) Huber, G. W.; O'Connor, P.; Corma, A. *Appl. Catal., A* **2007**, *329*, 120−129.
(4) Huber, G. W.; Iborra, S.; Corma, A. *Chem. Rev.* **2006**, *106*, 4044−4098.
(5) Kim, S. K.; Lee, H.-s.; Hong, M. H.; Lim, J. S.; Kim, J. *ChemSusChem* **2014**, *7*, 492−500.
(6) Kubička, D.; Šimáček, P.; Žilková, N. *Top. Catal.* **2009**, *52*, 161−168.
(7) Simácek, P.; Kubicka, D.; Sebor, G.; Pospíšil, M. *Fuel* **2009**, *88*, 456−460.
(8) Kubička, D.; Bejblová, M.; Vlk, J. *Top. Catal.* **2010**, *53*, 168−178.
(9) Simacek, P.; Kubicka, D.; Kubickova, I.; Homola, F.; Pospisil, M.; Chudoba, J. *Fuel* **2011**, *90*, 2473−2479.
(10) Kubička, D.; Horáček, J. *Appl. Catal., A* **2011**, *394*, 9−17.
(11) Snåre, M.; Kubicková, I.; Mäki-Arvela, P.; Chichova, D.; Eränen, K.; Murzin, D. Y. *Fuel* **2008**, *87*, 933−945.
(12) Gutierrez, A.; Kaila, R. K.; Honkela, M. L.; Slioor, R.; Krause, A. O. I. *Catal. Today* **2009**, *147*, 239−246.
(13) Morgan, T.; Grubb, D.; Santillan-Jimenez, E.; Crocker, M. *Top. Catal.* **2010**, *53*, 820−829.
(14) Veriansyah, B.; Han, J. Y.; Kim, S. K.; Hong, S.-A.; Kim, Y. J.; Lim, J. S.; Shu, Y.-W.; Oh, S.-G.; Kim, J. *Fuel* **2012**, *94*, 578−585.
(15) Snare, M.; Kubicckova, I.; Maki-Arvela, P.; Eranen, K.; Murzin, D. Y. *Ind. Eng. Chem. Res.* **2006**, *45*, 5708−5715.
(16) Immer, J. G.; Lamb, H. H. *Energy Fuels* **2010**, *24*, 5291−5299.
(17) Kim, S. K.; Han, J. Y.; Lee, H.-s.; Yum, T.; Kim, Y.; Kim, J. *Appl. Energy* **2014**, *116*, 199−205.
(18) Ren, H.; Yu, W.; Salciccioli, M.; Chen, Y.; Huang, Y.; Xiong, K.; Vlachos, D. G.; Chen, J. G. *ChemSusChem* **2013**, *6*, 798−801.
(19) Han, J.; Duan, J.; Chen, P.; Lou, H.; Zheng, X. *Adv. Synth. Catal.* **2011**, *353*, 2577−2583.
(20) Han, J.; Duan, J.; Chen, P.; Lou, H.; Zheng, X.; Hong, H. *Green Chem.* **2011**, *13*, 2561−2568.
(21) Han, J.; Duan, J.; Chen, P.; Lou, H.; Zheng, X.; Hong, H. *ChemSusChem* **2012**, *5*, 727−733.
(22) Hollak, S. A. W.; Gosselink, R. W.; van Es, D. S.; Bitter, J. H. *ACS Catal.* **2013**, *3*, 2837−2844.
(23) Sousa, L. A.; Zotin, J. L.; Teixeira da Silva, V. *Appl. Catal., A* **2012**, *449*, 105−111.
(24) Qin, Y.; Chen, P.; Duan, J.; Han, J.; Lou, H.; Zheng, X.; Hong, H. *RSC Adv.* **2013**, *3*, 17485−17491.
(25) Park, S.; Ruoff, R. S. *Nat. Nanotechnol.* **2009**, *4*, 217−224.
(26) Allen, M. J.; Tung, V. C.; Kaner, R. B. *Chem. Rev.* **2009**, *110*, 132−145.
(27) Stoller, M. D.; Park, S.; Zhu, Y.; An, J.; Ruoff, R. S. *Nano Lett.* **2008**, *8*, 3498−3502.
(28) Blake, P.; Brimicombe, P. D.; Nair, R. R.; Booth, T. J.; Jiang, D.; Schedin, F.; Ponomarenko, L. A.; Morozov, S. V.; Gleeson, H. F.; Hill, E. W.; Geim, A. K.; Novoselov, K. S. *Nano Lett.* **2008**, *8*, 1704−1708.
(29) Lin, Y.; Ding, F.; Yakobson, B. I. *Phys. Rev. B: Condens. Matter Mater. Phys.* **2008**, *78*, 041402.
(30) Dimitrakakis, G. K.; Tylianakis, E.; Froudakis, G. E. *Nano Lett.* **2008**, *8*, 3166−3170.
(31) Ataca, C.; Akturk, E.; Ciraci, S.; Ustunel, H. *Appl. Phys. Lett.* **2008**, *93*, 043123.

DOI: 10.1021/acscatal.5b00335
ACS Catal. 2015, 5, 3292−3303

(32) Yoon, D.; Chung, K. Y.; Chang, W.; Kim, S. M.; Lee, M. J.; Lee, Z.; Kim, J. *Chem. Mater.* **2014**, *27*, 266−275.
(33) Huang, C.; Li, C.; Shi, G. *Energy Environ. Sci.* **2012**, *5*, 8848−8868.
(34) Hummers, W. S.; Offeman, R. E. *J. Am. Chem. Soc.* **1958**, *80*, 1339−1339.
(35) Kovtyukhova, N. I.; Ollivier, P. J.; Martin, B. R.; Mallouk, T. E.; Chizhik, S. A.; Buzaneva, E. V.; Gorchinskiy, A. D. *Chem. Mater.* **1999**, *11*, 771−778.
(36) Kim, S. K.; Brand, S.; Lee, H.-s.; Kim, Y.; Kim, J. *Chem. Eng. J.* **2013**, *228*, 114−123.
(37) ASTM Standard D7213, ASTM International: West Conshohocken, PA, 2007, DOI: 10.1520/D7213-12E01, www.astm.org.
(38) Kresse, G.; Hafner, J. *Phys. Rev. B: Condens. Matter Mater. Phys.* **1994**, *49*, 14251−14269.
(39) Kresse, G.; Furthmüller, J. *Comput. Mater. Sci.* **1996**, *6*, 15−50.
(40) Kresse, G.; Joubert, D. *Phys. Rev. B: Condens. Matter Mater. Phys.* **1999**, *59*, 1758−1775.
(41) Perdew, J. P.; Burke, K.; Ernzerhof, M. *Phys. Rev. Lett.* **1996**, *77*, 3865−3868.
(42) Kresse, G.; Furthmüller, J. *Phys. Rev. B: Condens. Matter Mater. Phys.* **1996**, *54*, 11169−11186.
(43) Grimme, S. *J. Comput. Chem.* **2006**, *27*, 1787−1799.
(44) Parthe, E.; Sadogopan, V. *Acta Crystallogr.* **1963**, *16*, 202−205.
(45) Zhou, X.; Huang, X.; Qi, X.; Wu, S.; Xue, C.; Boey, F. Y. C.; Yan, Q.; Chen, P.; Zhang, H. *J. Phys. Chem. C* **2009**, *113*, 10842−10846.
(46) Budi Nursanto, E.; Nugroho, A.; Hong, S.-A.; Kim, S. J.; Yoon Chung, K.; Kim, J. *Green Chem.* **2011**, *13*, 2714−2718.
(47) Seo, M.; Yoon, D.; Hwang, K. S.; Kang, J. W.; Kim, J. *Carbon* **2013**, *64*, 207−218.
(48) Aegerter, P. A.; Quigley, W. W. C.; Simpson, G. J.; Ziegler, D. D.; Logan, J. W.; McCrea, K. R.; Glazier, S.; Bussell, M. E. *J. Catal.* **1996**, *164*, 109−121.
(49) Choi, J.-S.; Krafft, J.-M.; Krzton, A.; Djéga-Mariadassou, G. *Catal. Lett.* **2002**, *81*, 175−180.
(50) Sayag, C.; Benkhaleda, M.; Suppanb, S.; Trawczynskib, J.; Djéga-Mariadassoua, G. *Appl. Catal., A* **2004**, *275*, 15−24.
(51) Sing, K. S. *Pure Appl. Chem.* **1985**, *57*, 603−619.
(52) Plourde, M.; Belkacemi, K.; Arul, J. *Ind. Eng. Chem. Res.* **2004**, *43*, 2382−2390.
(53) Rozmysłowicz, B.; Mäki-Arvela, P.; Tokarev, A.; Leino, A.-R.; Eränen, K.; Murzin, D. Y. *Ind. Eng. Chem. Res.* **2011**, *51*, 8922−8927.
(54) Peng, B.; Yuan, X.; Zhao, C.; Lercher, J. A. *J. Am. Chem. Soc.* **2012**, *134*, 9400−9405.
(55) Hwu, H. H.; Chen, J. G. *Chem. Rev.* **2004**, *105*, 185−212.
(56) Stottlemyer, A. L.; Kelly, T. G.; Meng, Q.; Chen, J. G. *Surf. Sci. Rep.* **2012**, *67*, 201−232.
(57) Kim, S. K.; Han, J. Y.; Hong, S.-A.; Lee, Y.-W.; Kim, J. *Fuel* **2013**, *111*, 510−518.
(58) Dąbek, L.; Świątkowski, A.; Dziaduszek, J. *Environ. Prog.* **2007**, *26*, 360−364.
(59) Georgi, A.; Kopinke, F.-D. *Appl. Catal., B* **2005**, *58*, 9−18.

DOI: 10.1021/acscatal.5b00335
ACS Catal. 2015, 5, 3292−3303